Indian Journal of Chemistry
Vol. 58A, August 2019, pp. 867-873

# $CeO_2$ nanowires inserted into reduced graphene oxide as active electrocatalyst for oxygen reduction reaction

Yabo Sun[b], Yuanyuan Chu[a,b,c,]*, Xiaoming Xia[b], Haitao Wang[b], Xiaoyao Tan[a,b,]*, Zhao Dai[b] & Liang Wang[a]

[a]State Key Laboratory of Separation Membranes and Membrane Processes, Tianjin Polytechnic University,
No.399 Binshui West Road, Tianjin 300387, China
[b]School of Environmental and Chemical Engineering, Tianjin Polytechnic University, No.399 Binshui West Road, Tianjin 300387, China
[c]Tianjin Key Laboratory of Advanced Fibers and Energy Storage, Tianjin Polytechnic University, No.399 Binshui West Road,
Tianjin 300387, China
Email: chuyuanyuan1982@163.com

*Received 20 August 2018; revised and accepted 24 June 2019*

Fabrication of an interconnected and conductive nano-architecture has been a prospective strategy to design a high-performance and low cost electrocatalyst for oxygen reduction reaction (ORR). Herein, a novel nano-architecture assembled by graphene nanosheets and $CeO_2$ nanowires (NWs) with a hierarchical structure has been developed by a facile hydrothermal process using ethanol/water as solvents without any organic additives. In this framework, graphene oxide (GO) has been reduced to graphene and chemical bonding formed between the GO and $CeO_{2\ NWs}$ in a hydrothermal process. The imbedded $CeO_{2\ NWs}$ has been prevent the restacking of the graphene sheets and improved the electrical conductivity of the hybrid catalyst. The effect of different ratios of GO to $CeO_{2\ NWs}$ in the hybrid have been studied. The $rGO_3$-$CeO_{2\ NWs}$ composite exhibited better catalytic performance with slow attenuation and high limiting current density 3.55 and 1.99 times higher than $CeO_{2\ NWs}$ and pure GO. The onset potential of $rGO_3$-$CeO_{2\ NWs}$ is 0.13 V and 0.05 V positive shift from that of $CeO_{2\ NWs}$ and pure GO, respectively, suggesting that the $rGO_3$-$CeO_{2\ NWs}$ hybrid has been an excellent stability and activity for ORR. It has been found that $CeO_{2\ NWs}$ served not only as an effective catalyst but also as an “oxygen buffer” to relieve oxygen insufficiency for ORR.

**Keywords:** $CeO_2$ nanowires, Reduced graphene oxide, Synergistic effects, Oxygen reduction reaction

Sustainable energy storage and conversion technologies have been extensively developed due to the rapid depletion of fossil fuels and harmful emissions of carbon to the atmosphere[1]. Polymer electrolyte membrane fuel cells (PEMFCs) can convert chemical energy into electrical energy with high efficiency of power generation and cleanly emission, which has been the focus in cogeneration systems and vehicle applications[2,3]. Pt and other precious metal catalysts have been considered as the best electrocatalysts for oxygen reduction reaction (ORR), they still suffer from the sluggish ORR kinetics, susceptibility to time-dependent stability and CO poisoning[4,5], which seriously reduce the cathode potential and decrease fuel efficiency. For these problems, highly active and durable electrocatalysts for the ORR have long been the key to the performance of PEMFCs and their commercialization. Over the past few years, much effort had been devoted to the development of different types of non-noble metal catalysts such as metal-based complexes (Fe and Co)[6-8], transition metal oxides (sulfides)[9-11], nitrides[12,13], and heteroatom-doped carbon materials[14,15].

Recently, transition metal oxides[16-19] such as $TiO_2$, $Fe_3O_4$, $MnO_2$ and $Co_3O_4$ have been well studied as promising candidates for high-performance cathodes in PEMFCs due to abundant hydroxyl groups on the surfaces of the transition metal oxides, low cost, acid-base resistance property and high stability. $CeO_2$ serves as one of the most important systems because of the variable valence states of Ce cations and a high oxygen storage capacity. However, poor ionic mobility and low electrical conductivity of transition metal oxides need to be resolved by synthesizing nanomaterials with diverse shapes, porous or interconnected structure and composited with conductive carbon materials. Nowadays, incorporation of transition metal oxides with carbon-based materials such as amorphous carbons[20], carbon nanotubes (CNT)[21], graphene nanosheets[22], is an effective strategy to enhance the electrical conductivity and reduce the agglomeration of metal oxides during the electrochemical cycling, favoring the long-term stability of the fuel cells. It is well known that one-dimensional (1D) nanowires and nanotubes (NTs) have demonstrated excellent performance due to their unique 1D morphologies and high surface area.

Herein, we report design and synthesis of a novel interconnected nano-architecture assembled by graphene nanosheets and $CeO_{2\ NWs}$. Such a hybrid can be profited from the synergistic effects of each component including (i) The imbedded $CeO_{2\ NWs}$ effectively inhibiting the graphene from restacking and restraining the coiled or folded GO sheets to provide more channels for electron conduction; (ii) Creating oxygen vacancies to generate localized electrons on the surface to induce an intimate contact between GO sheets and $CeO_{2\ NWs}$, and (iii) Porous structure for fuel transport compared with those of pure GO and $CeO_{2\ NWs}$.

## Materials and Methods

### Preparation of rGO-$CeO_{2\ NWs}$ hybrids

$CeO_{2\ NWs}$ were synthesized according to a modified hydrothermal method[23]. $CeCl_3.7H_2O$ (0.2515 g) and NaCl (0.523 g) were dissolved in water (6 mL) by sonication. Then, 7.5 mL of NaOH solution (12 M) was injected into the suspension. The suspension was stirred and heated at 180 °C for 30 h in a 25 mL Teflon-lined stainless steel autoclave. The products were washed with deionized (DI) water and dried at 50 °C. Finally, the dried products were calcined at 300 °C for 1 h. GO was obtained by a modified Hummers' method[24].

A hydrothermal method was employed to synthesize rGO-$CeO_{2\ NWs}$ composites[25]. About 60 mg GO and $CeO_{2\ NWs}$ mixture in varying ratios was uniformly mixed with a solution of ethanol/water (1:1) by sonication and stirring, until a homogeneous suspension was achieved. The suspension was transferred to a Teflon-lined autoclave (100 mL) and heated at 120 °C for 4 h. The reduction of GO could be achieved using ethanol as a reductant. rGO-$CeO_{2\ NWs}$ nanocomposites were purified by centrifugation, washed with DI water and dried under vacuum at 60 °C for 12 h. The composites at other different graphene to $CeO_{2\ NWs}$ ratios were : 40 mg-20 mg, 45 mg-15 mg and 48 mg-12 mg labeled[26] as $rGO_2$-$CeO_{2\ NWs}$, $rGO_3$-$CeO_{2\ NWs}$ and $rGO_4$-$CeO_{2\ NWs}$.

### Characterization

#### *Structure Characterization*

XRD data of the catalysts were collected using a D/max-r B diffractometer (Japan) using a Cu Kα X-ray source operating at 45 kV and 100 mA, scanning at a rate of 8° $min^{-1}$ with an angular resolution of 0.05° of $2\theta$ scan. Scanning electron microscopy (SEM) images were taken on a Leo 1530 field-emission scanning electron microscope. X-ray photoelectron spectroscopy (XPS) was used to determine the chemical state of Pt and Ru with a physical electronics PHI model 5700 instrument.

#### *Electrochemical Activity Characterization*

All the electro-chemical measurements were conducted using CHI 760E electro-chemical workstation, with a conventional three-electrode setup at 25 °C working electrodes with the catalysts were prepared as follows. A conventional three electrode cell was employed with a platinum wire as the counter electrode, a saturated Hg/HgO electrode as the reference electrode, and a glassy carbon (GC) electrode (diameter = 5 mm) with coated catalysts serving as the working electrode. The catalyst ink was produced by mixing 5 mg of the catalyst under sonication for 30 min in 2.5 mL of ethanol. The suspension (5 µL) was transferred to the surface of the polished glassy carbon electrode and dried in the air at room temperature, then covered with Nafion. The above three electrodes and a 0.1 M KOH solution were used to form a three-electrode system for electrochemical measurements. CV (Cyclic Voltammetry) tests were performed in $N_2$ and $O_2$ saturated electrolytes. LSV (linear sweep voltammetry) tests were performed at a rotating rate varying from 500 to 2500 rpm. To check $CH_3OH$ tolerance of the prepared samples, 20000 ppm $CH_3OH$ was added to the electrolyte, and another LSV test was performed at 1600 rpm.

## Results and Discussion

SEM images of $CeO_{2\ NWs}$, GO and $rGO_3$-$CeO_{2\ NWs}$ hybrid are shown in Fig. 1. It can be seen from Fig. 1a that the fairly uniform $CeO_{2\ NWs}$ was obtained with diameter (20–35 nm) and length (1–3 µm). SEM images of pure GO (Fig. 1b) is exhibiting much clearly visible wrinkles with multilayer and rougher surfaces. As demonstrated in Fig. 1c and Fig. 1d, the $rGO_3$-$CeO_{2\ NWs}$ hybrid is constructed from uniform 1D $CeO_{2\ NWs}$ and thin-layered graphene nanosheets. The $CeO_{2\ NWs}$ were closely threaded through the thin graphene layers, leading to the formation of an interlaced three-dimensional conductive network. EDS-mapping spectra (Fig. 1e–1h) exhibited a homogeneous dispersion of the catalyst, confirming the uniform distributions of Ce (in blue), C (in green) and O (in red) along the 1D CeO$_{2\ \mathrm{NWs}}$, suggesting the well dispersed CeO$_{2\ \mathrm{NWs}}$ with graphene could restrain the wrinkle of GO.

For the crystal structure of the as-prepared catalysts, as illustrated in Fig. 2, XRD of GO showed the typical diffraction peak at an angel of 11.3° for the (001) plane due to the formation of the oxygen-containing functional groups on the surface of the GO sheets[26]. The as-prepared rGO-CeO$_{2\ \mathrm{NWs}}$ composites with a different ratio displayed a broad and weak diffraction peak at 24.6°, arising from the (002) reflection of GO sheets, confirming the existence of reduced graphene oxide. However, the diffraction peaks attributing to graphite carbon for the (001) plane could be observed with the increased CeO$_{2\ \mathrm{NWs}}$ content in the XRD patterns of rGO-CeO$_{2\ \mathrm{NWs}}$ composites, which may be attributed to the low intensity and low mass ratio as well as the formation of threaded CeO$_{2\ \mathrm{NWs}}$ on the graphene surface. Meanwhile, the intense peaks at $2\theta$ = 28.6°, 33.2°, 47.5°, 56.6°, 58.9°, 66.9°, 76.9° and 79.1° can be indexed to (111), (200), (220), (311), (222), (400), (331) and (420) reflections of crystalline CeO$_2$ (JCPDS 81-0792), respectively.

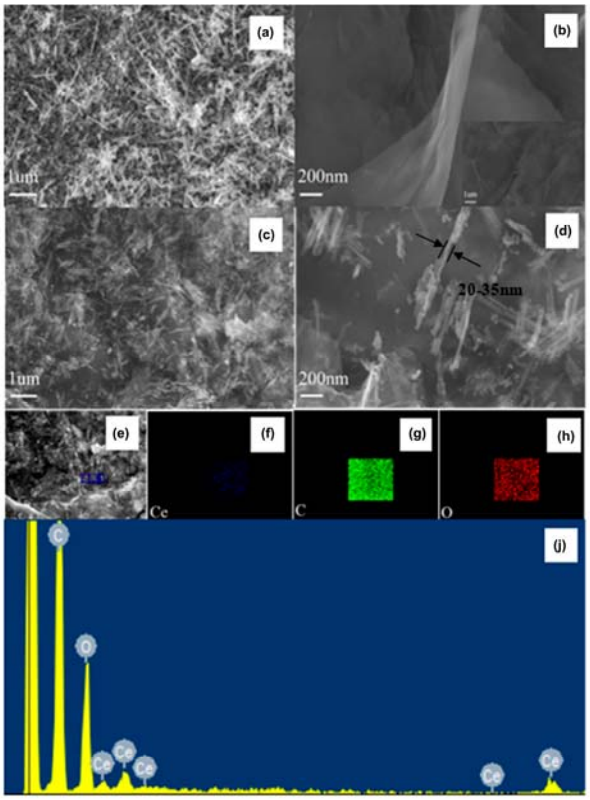

Fig.1 — SEM image of (a) CeO$_{2\ \mathrm{NWs}}$, (b) pure GO and (c-d) GO$_3$-CeO$_{2\ \mathrm{NWs}}$ hybrid structure, (e-h) EDS-mapping spectra, Ce (in blue), C (in green) and O (in red) and (j) EDS analysis of rGO$_3$-CeO$_{2\ \mathrm{NWs}}$.

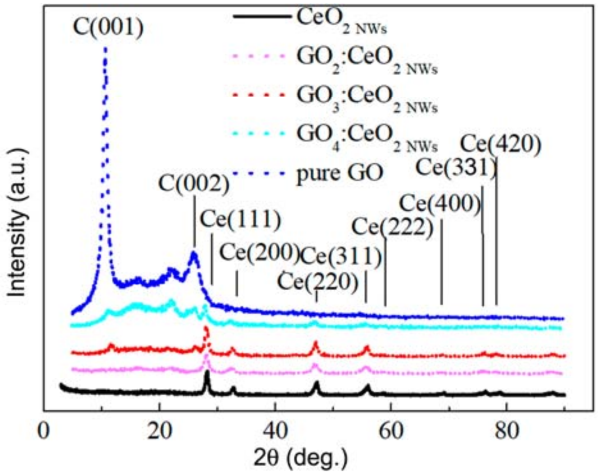

Fig.2 — XRD patterns of CeO$_{2\ \mathrm{NWs}}$, pure GO and rGO-CeO$_{2\ \mathrm{NWs}}$ hybrid composites with different ratio.

X-ray photo-electron spectroscopy (Fig. 3) illustrated the compositions of rGO$_3$-CeO$_{2\ \mathrm{NWs}}$ composite and the mechanism of the interactions between GO$_3$ and CeO$_{2\ \mathrm{NWs}}$. The full survey of rGO$_3$-CeO$_{2\ \mathrm{NWs}}$ hybrid displays the signals of Ce 3d, O 1s, and C 1s in the range of 0–1400 eV in Fig. 3a, confirming the successful recombination of GO and CeO$_{2\ \mathrm{NWs}}$. The deconvolution peaks of Ce 3d, O 1s, and C 1s are shown in Fig. 3b, 3c, and 3d, respectively. For Ce 3d peaks (Fig. 3b), four featured peaks locating at 883.7, 889.7, 890.2, and 901.8 eV depict the Ce element chemical states, and fingerprint peak at 917.6 eV is the strong evidence for the presence of Ce$^{4+}$, and the peaks located at 886.6 and 904.5 eV are the typical peaks[27,28] of Ce$^{3+}$. The Ce3d spectrum revealed the coexistence of Ce$^{3+}$ and Ce$^{4+}$ species with Ce$^{4+}$ being the main valence state in the rGO$_3$-CeO$_{2\ \mathrm{NWs}}$ hybrid. It is known that the change of valence state of CeO$_2$ from Ce$^{4+}$ to Ce$^{3+}$ will introduce oxygen vacancies and unsaturated chemical bond, which activates oxygen in the redox processes, and makes the charge transfer from mobile holes in graphene layers to localized electrons on CeO$_{2\ \mathrm{NWs}}$, thus leading to the great improvement in oxygen reduction on the rGO$_3$-CeO$_{2\ \mathrm{NWs}}$ catalyst[29-31]. The C1s spectra (Fig. 3c) displayed the presence of nonoxygenated carbon at 285.3 eV (C=C/C-C), epoxy group at 287.6 eV (C=O), and ester group[32] at 289.3 eV (O-C=O) The content of nonoxygenated carbon increased due to a successful reduction of GO in the composite. Spectrum of the O1s (Fig. 3d) was deconvoluted into the carboxylate and ester group (C-OH at 533.7 eV and O-C=O at 531.7 eV), which is

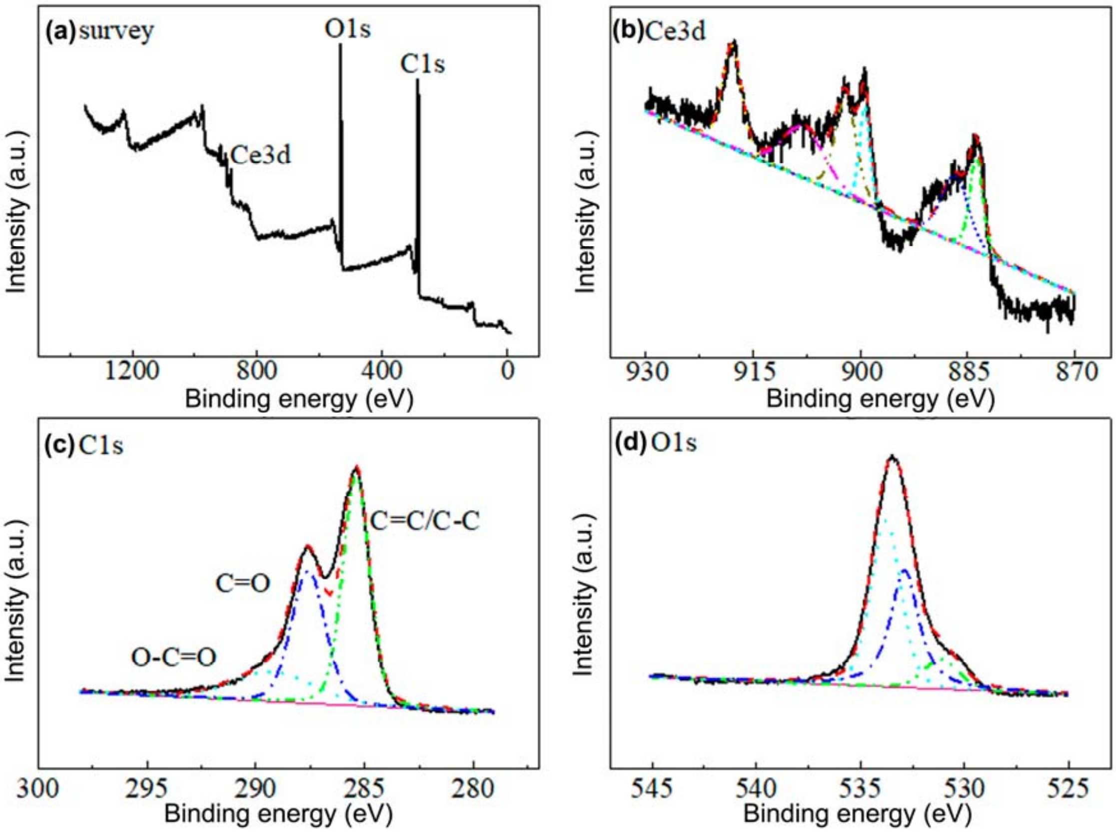

Fig.3 — (a) Survey spectra of catalyst for $rGO_3$-$CeO_2$ $_{NWs}$ hybrid composite, and deconvolution of peaks (b) Ce 3d, (c) C1s, and, (d) O 1s spectrum.

in accordance with the above C1s spectra and a new peak locating at 531.0 eV corresponding to the Ce-O bond gives a very strong evidence for the presence of electron transfer[27, 28, 33] between GO and $CeO_2$. The peaks at 531.0 and 531.7 eV belong to the lattice oxygen whereas the one at 533.7 eV corresponds to the chemisorption oxygen[33] such as –OH. The improvement of the redox performance for the catalyst maybe derived from the transformation between oxide species and favored the electron transfer[34].

Rotating disk electrode (RDE) technology was used to evaluate the electrocatalytic activity of catalysts. The LSV curves for different samples at a rotating speed of 1600 rpm are shown in Fig. 4a. It can be seen that $CeO_2$ $_{NWs}$ and pure GO catalysts exhibited a very low ORR electrocatalytic activity. Incorporation of $CeO_2$ $_{NWs}$ with pure GO and introduction of heterogeneous contact-interface between them resulted in a remarkably increased the diffusion-limited current density and the highest value reached on $rGO_3$-$CeO_2$ $_{NWs}$ at 1600 rpm. In addition, positive shifts at 0.13 V and 0.05 V were observed for onset potential on $rGO_3$-$CeO_2$ $_{NWS}$ (onset potential of 0.91 V vs. RHE) compared to $CeO_2$ $_{NWS}$ (onset potential of 0.78 V vs. RHE) and pure GO (onset potential of 0.86 V vs. RHE) catalysts, respectively, indicating enhanced ORR performance. $rGO_3$-$CeO_2$ $_{NWs}$ hybrid contained more active sites and more easily accessible to adsorb $O_2$, making a great contribution to catalytic activities. The Tafel slopes in Fig. 4b were obtained from the linear plots of LSV to comprehensively understand the difference of ORR kinetics among rGO-$CeO_2$ $_{NWs}$ hybrids, $CeO_2$ $_{NWs}$ and pure GO. A slope of 56.0 mV $dec^{-1}$ can be observed for $rGO_3$-$CeO_2$ $_{NWs}$, which is much lower than that of $CeO_2$ $_{NWs}$ (98.34 mV $dec^{-1}$), pure GO (83.35 mV $dec^{-1}$) and Pt/C (79.2 mV $dec^{-1}$)[35], suggesting a much better kinetic behavior for ORR. Also, the electron-transfer resistance of $rGO_3$-$CeO_2$ $_{NWs}$ hybrid showed the smallest semicircle according to the electrochemical impedance spectra (EIS) presented in Fig. 4c, indicating the hybrid could efficiently enhance the conductivity and improve the catalytic activity for ORR due to the synergetic chemical coupling between GO and $CeO_2$ $_{NWs}$. Furthermore, the durability of the rGO-$CeO_2$ $_{NWs}$ hybrid, $CeO_2$ $_{NWs}$ and

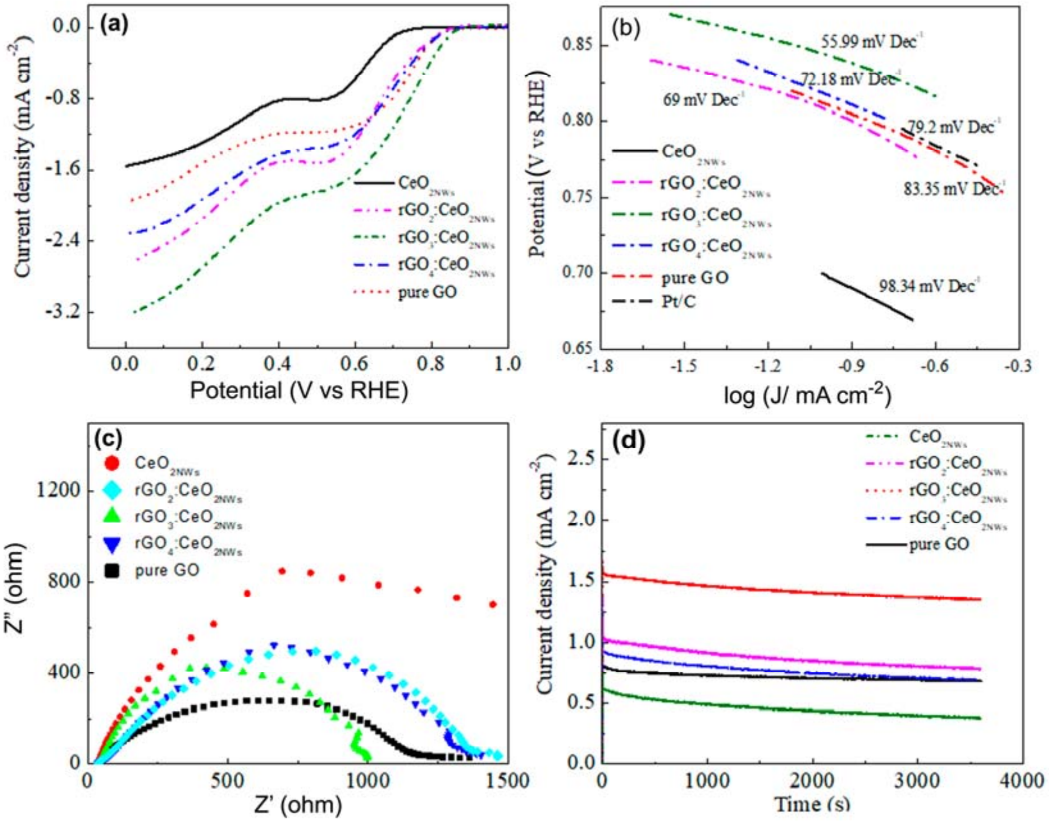

Fig. 4 — (a) LSV curves of rGO-$CeO_2$ $_{NWs}$ hybrid composites, $CeO_2$ $_{NWs}$ and pure GO; (b) Tafel plot of kinetic current for different catalysts; (c) Nyquist plots obtained from EIS of different catalysts; (d) *i-t* curves for the different sample at 0.625 V. Supporting electrolyte: 0.1 M KOH Scan rate: 10 mV s$^{-1}$.

pure GO were evaluated by *i-t* curves (Fig. 4d). It was observed that the response of the $rGO_3$-$CeO_2$ $_{NWs}$ hybrid exhibited a very slow attenuation with a high current retention after 3600 s, which is 3.55 and 1.99 times higher than $CeO_2$ $_{NWs}$ and pure GO, suggesting that the $rGO_3$-$CeO_2$ $_{NWs}$ hybrid had an excellent stability. $CeO_2$ $_{NWs}$ can serve not only as an effective catalyst but also as an "oxygen buffer" to relieve oxygen insufficiency for ORR.

We further studied the ORR catalytic activities of $rGO_3$-$CeO_2$ $_{NWs}$ hybrid in $N_2$- and $O_2$-saturated 0.1 M aqueous KOH electrolyte solutions by CV curves at a scan rate of 50 mV s$^{-1}$ (Fig. 5a). In $N_2$-saturated solution, the CV curve presented no obvious reduction peak between 0 and 1.2 V. In contrast, when $O_2$ was saturated in the electrolyte, the curve presented a clear increase in current density at around 0.92 V, suggesting the remarkable ORR performance. In the meantime, RDE measurements also exhibited that the diffusion-limited current density on $rGO_3$-$CeO_2$ $_{NWs}$ hybrid increased with increasing rotation rate from 500 to 2500 rpm (Fig. 5b). The onset ORR potential is kept almost constant at around 0.91 V within the rotation rate. The corresponding Koutecky-Levich (K-L) plots on the $rGO_3$-$CeO_2$ $_{NWs}$ hybrid (Fig. 5c) demonstrated the inverse current density $(-J)^{-1}$ as a function of the inverse of the square root of the rotation speed ($\omega^{-1/2}$) at several potentials. The transferred electron numbers per $O_2$ and kinetic current density in the ORR were determined by the Koutechy-Levich equation[36, 37].

$$\frac{1}{J}=\frac{1}{J_k}+\frac{1}{B\omega^{1/2}} \qquad \dots (1)$$

$$B = 0.2\,nFC_0D_0^{2/3}\gamma^{-1/6} \qquad \dots (2)$$

where $J$ is the measured current density and $J_k$ is the kinetic current density. $n$ represents the overall number of electrons gained per $O_2$, $F$ is the Faraday constant (96485 C mol$^{-1}$), $C_0$ is the bulk concentration of $O_2$ ($1.1\times10^{-3}$ mol L$^{-3}$), $D_0$ is the diffusion coefficient of $O_2$ in 0.1 M KOH ($1.9\times10^{-5}$ cm$^2$ s$^{-1}$) and $\gamma$ is the kinetic viscosity of the electrolyte (0.01 cm$^2$ s$^{-1}$). The constant 0.2 was adopted when the rotation rate was expressed in rpm. Remarkable enough, the electron transfer number n for ORR at the

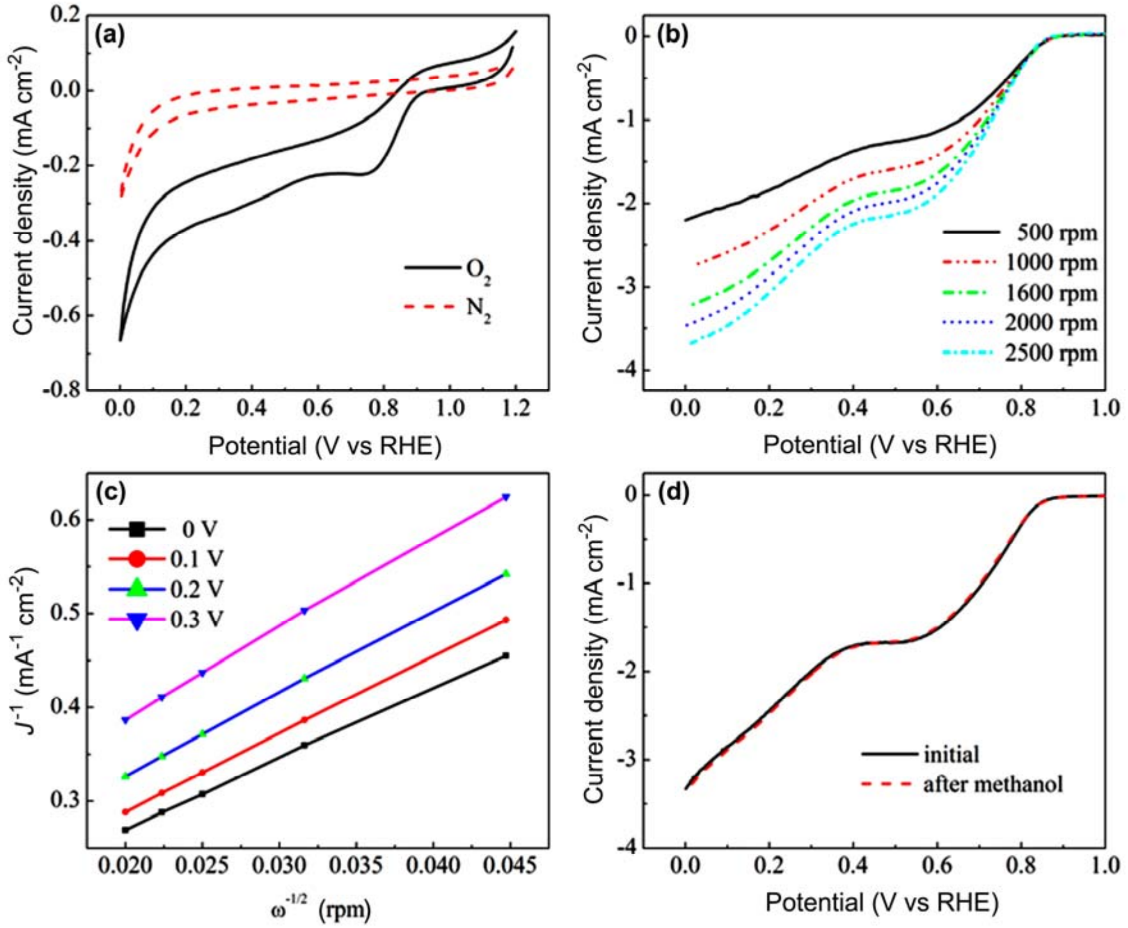

Fig.5 — (a) CV curves of ORR on the rGO$_3$-CeO$_{2\ \mathrm{NWS}}$ hybrid composite electrodes in N$_2$- and O$_2$-saturated 0.1 M KOH at a scan rate of 10 mV s$^{-1}$, (b) LSV curves at various rotating ration at a scan rate of 10 mV s$^{-1}$, (c) Koutecky-Levich plots at 0, 0.1, 0.2 and 0.3 V, and, (d) rGO$_3$-CeO$_{2\ \mathrm{NWS}}$ hybrid composite in O$_2$-saturated 0.1 M KOH solution with and without CH$_3$OH.

rGO$_3$-CeO$_{2\ \mathrm{NWs}}$ hybrid catalyst was calculated as 2.92–3.75 from 0 to 0.3 V (vs. RHE), which revealed that the electrocatalytic process of rGO$_3$-CeO$_{2\ \mathrm{NWs}}$ hybrid is almost a four-electron pathway for ORR and favorable for most cathodic reaction for a fuel cell. It is known that the methanol tolerance is an important factor for the catalyst especially in a direct methanol fuel cell (DMFC) since the methanol crossover effects lead to a seriously reduced performance for fuel cells. Addition of 1 M methanol to the O$_2$-saturated electrolyte does not because a significant decrease in onset potential for rGO$_3$-CeO$_{2\ \mathrm{NWs}}$ hybrid as shown in Fig. 5d, indicating it is free of poisoning effects from methanol and an excellent non-precious catalyst towards ORR.

## Conclusions

We have developed a facile hydrothermal approach to fabricate rGO$_x$-CeO$_{2\ \mathrm{NWs}}$ hybrids as an ORR electrocatalytic catalyst. The ORR activity of rGO$_3$-CeO$_{2\ \mathrm{NWs}}$ significantly favored a four-electron pathway in the ORR due to the synergistic effect between GO and CeO$_{2\ \mathrm{NWs}}$. The rGO$_3$-CeO$_{2\ \mathrm{NWs}}$ hybrids showed a very slow attenuation with a high current retention and remarkable increased the diffusion-limited current density at 1600 rpm compared to CeO$_{2\ \mathrm{NWs}}$ and pure GO, as well as its free of poisoning effects from methanol towards ORR. The increased conductivities and catalytic activity were ascribed to the synergetic chemical coupling between GO and CeO$_{2\ \mathrm{NWs}}$, and CeO$_{2\ \mathrm{NWs}}$ served not only as an effective catalyst but also as an “oxygen buffer” to relieve oxygen insufficiency for ORR. The strategy of using GO and CeO$_{2\ \mathrm{NWs}}$ hybrid as a catalyst with high performance and low cost provides a potential candidate for fuel cells.

## Acknowledgement

The present work is financially supported by the National Natural Science Foundation of China (Grant

No. 21206124, No. 21506159, No. 51478314 and No. 51638011), National Key Research and Development Plan (2016YFC0400503, 2016YFC0400506), Natural Science Foundation of Tianjin (No.12JCZDJC28400 and No.12JCQNJXC-7208600), and the Science and Technology Plans of Tianjin (No. 15PTSYJC00230).

## References

1 Luo J, Im J H, Mayer M T, Schreier M, Nazeeruddin M K, Park N G, Tilley S D, Fan H J & Graetzel M, *Sci*, 345 (2014) 1593.

2 Springer T E, Zawodzinski T A & Gottesfeld S, *J Electrochem Soc*, 138 (1991) 2334.

3 Steele B C H & Heinzel A, *Nature*, 414 (2001) 345.

4 Zhu C Z & Dong S J, *Nanoscale*, 5 (2013) 1753.

5 Bai X, Shi Y, Guo J, Gao L, Wang K, Du Y & Ma T, *J Power Sources*, 306 (2016) 85.

6 Lin L, Zhu Q & Xu A W, *J Am Chem Soc*, 136 (2014) 11027.

7 Wen Z, Ci S, Zhang F, Feng X, Cui S, Mao S, Luo S & He Z, *Adv Mater,* 24 (2012) 1399.

8 Mamlouk M, Kuma S M S & Gouerec P, *J Power Sources*, 196 (2011) 7594.

9 Cheng F, Su Y, Liang J, Tao Z & Chen J, *Chem Mater*, 22 (2010) 898.

10 Wu Z S, Yang S, Sun Y, Parvez K, Feng X & Mullen K, *J Am Chem Soc*, 134 (2012) 9082.

11 Wang H, Liang Y, Li Y & Dai H, *Angew Chem Int Ed Engl*, 50 (2011) 10969.

12 Dong Y Z, Wu Y M, Liu M J & Li J H, *Chemsuschem*, 6 (2013) 2016.

13 Liu M, Dong Y, Wu Y, Feng H & Li J, *Chemistry*, 19 (2013) 14781.

14 Gong Y, Fei H, Zou X, Zhou W, Yang S, Ye G, Liu Z, Peng Z, Lou J, Vajtai R, Yakobson B I, Tour J M & Ajayan P M, *Chem Mater*, 27 (2015) 1181.

15 Wohlgemuth S A, White R J, Willinger M G, Titirici M M & Antonietti M, *Green Chem*, 14 (2012) 1515.

16 Guo L M, Liang K, Marcus K, Li Z, Zhou L, Mani P D, Chen H, Shen C, Dong Y J, Zhai L, Coffey K R, Orlovskaya N, Sohn Y H & Yang Y, *ACS Appl Mater Inter*, 8 (2016) 34970.

17 Almeida I, Mendo S G, Carvalho M D, Correia J P & Viana A S, *Electrochimica Acta*, 188 (2016) 1.

18 Yu Q, Xu J, Wu C, Zhang J & Guan L, *ACS Appl Mater Inter*, 8 (2016) 35264.

19 Liu K, Huang X, Wang H, Li F, Tang Y, Li J & Shao M, *ACS Appl Mater Inter,* 8 (2016) 34422.

20 Zhang C, Wang B, Shen X, Liu J, Kong X, Chuang S S C, Yang D, Dong A & Peng Z, *Nano Energy*, 30 (2016) 503.

21 Zhao S & Rasimick B, Mustain W & Xu H, *Appl Catal B: Environ*, 203 (2017) 138.

22 Kong D, Yuan W, Li C, Song J, Xie A & Shen Y, *Appl Surf Sci*, 393 (2017) 144.

23 Ke J, Xiao J W, Zhu W, Liu H, Si R, Zhang Y W & Yan C H , *J Am Chem Soc*, 135 (2013) 15191.

24 Hummers Jr W H & Offeman R E, *J Am Chem Soc*, 80 (1958) 1339.

25 Yu S, Liu Q, Yang W, Han K, Wang Z & Zhu H, *Electrochim Acta*, 94 (2013) 245.

26 Park S, Lee K S, Bozoklu G, Cai W, Nguyen S T & Ruoff R S, *ACS nano*, 2 (2008) 572.

27 Shan W P, Liu F D, He H, Shi X Y & Zhang C B, *Appl Catal B-Environ*, 115 (2012) 100.

28 Fang J, Bi X Z, Si D J, Jiang Z Q & Huang W X, *Appl Surf Sci*, 253 (2007) 8952.

29 Wohlgemuth S A, White R J, Willinger M G, Titirici M M & Antonietti M, *Green Chem,* 14 (2012) 1515.

30 Zhu W J, Zhang J, Gong X Q & Lu G, *Cataly Today*, 165 (2011) 19.

31 Joung D, Singh V, Park S, Schulte A, Seal S & Khondaker S I, *J Phys Chem C*, 115 (2011) 24494.

32 Cong H P, Ren X C, Wang P & Yu S H, *ACS Nano*, 6 (2012) 2693.

33 Gao F Y, Tang X L, Yi H H, Li J Y, Zhao S Z, Wang J G, Chu C & Li C L, *Chem Eng J*, 317 (2017) 20.

34 Lu X, Song C, Chang C C, Teng Y, Tong Z & Tang X, *Ind Eng Chem Res,* 53 (2014) 11601.

35 Jin H, Huang H, He Y, Feng X, Wang S, Dai L & Wang J, *J Am Chem Soc*, 137 (2015) 7588.

36 Liang Y, Wang H, Zhou J, Li Y, Wang J, Regier T & Dai H, *J Am Chem Soc*, 134 (2012) 3517.

37 Xiong W, Du F, Liu Y, Jr. A P, Supp M, Ramakrishnan T S, Dai L & Jiang L, *J Am Chem Soc,* 132 (2010) 15839.